





36 water cycle (Edokossi et al., 2020; Lin et al., 2018; Ma et al., 2021; Pipatsitee et al., 2023). Therefore, RT  
37 and high-precision ZTD can be used to provide rapid and accurate tropospheric correction services in space  
38 geodesy while benefiting weather forecasting and climate change research (Crocetti et al., 2024; He et al.,  
39 2024).

40 GNSS is an important means of water vapor detection and is increasingly important in short-term and near-  
41 space forecasting (Eugenia Bianchi et al., 2016; Li et al., 2015; Sha et al., 2024). GNSS-ZTD retrieval has an  
42 excellent prospect for development due to the advantages of all-weather, RT, and high accuracy (Hadas et  
43 al., 2020; Lu et al., 2016; Pan et al., 2024). The double-difference algorithm through GNSS networking and  
44 PPP is commonly used for ZTD retrieval (Stepniak et al., 2022). PPP has a broader range of applications,  
45 including timing, atmospheric modeling, and deformation monitoring, due to the lower cost and one GNSS  
46 receiver (Ge et al., 2021; Liu et al., 2018; Wang et al., 2023). However, the PPP technology relies on high-  
47 precision GNSS orbit and clock error products, typically released as final precise post-processing products  
48 to the public (Li et al., 2022). A working group was established by the IGS to study GNSS RT data and  
49 launched an RT data service in 2013 for high-precision RT-PPP applications (Gu et al., 2022). GNSS RT  
50 orbits and clock corrections are made available to users based on the Internet through the Networked  
51 Transport of RTCM via Internet Protocol (NTRIP) (Shu et al., 2024; Wang et al., 2018; Wang et al., 2018).  
52 SSR products have led to a remarkable 50% improvement in RT-PPP positioning accuracy compared to IGS  
53 ultra-fast products (Elsobeiey et al., 2016). SSR products are becoming increasingly abundant with the rapid  
54 development of computer arithmetic and the increasing demand for real-time high-precision GNSS  
55 applications. Li and Wang (Li et al., 2022) conducted a comprehensive evaluation of SSR products from 10  
56 ACs multi-GNSS and performed RT dynamic PPP, which showed the most complete and highest quality  
57 products obtained by CNES and WHU. Furthermore, it has also been applied to RT deformation monitoring,  
58 RT atmospheric detection, and other fields (Li et al., 2023). Capilla et al. (2016) applied RT-PPP to  
59 deformation monitoring and demonstrated that the technique has a monitoring accuracy of 2 cm and proved  
60 that RT-PPP was full of potential for deformation monitoring applications. Li et al. (2015) investigated the  
61 ZTD solution and Integrated Water Vapor (IWV) retrieval of multi-GNSS RT-PPP. They compared RT-PPP-  
62 derived ZTD with data from concurrent radiosonde stations and VLBI, which demonstrated that the  
63 performance of the multi-GNSS RT-PPP-derived ZTD can reach the millimeter level and has potential in the  
64 application of meteorology.

65 Researchers have assessed the accuracy of single-system RT-PPP-derived ZTD and multi-GNSS RT-PPP-  
66 derived ZTD. Lu et al. (2015) found that the retrieval accuracy of atmospheric water vapor can be improved  
67 by several millimeters when a combined GPS and BDS solution is used. Li et al. (2015) obtained RT-PPP-  
68 derived ZTD using GPS, BDS2, Galileo, and GLONASS PPP, demonstrating higher accuracy and greater  
69 ZTD availability than a single-system PPP. Jiao et al. (2019) analyzed the results of PPP and multi-GNSS  
70 PPP, noting that the positioning accuracy and convergence were significantly improved with the inclusion of  
71 the BDS3 satellite system. The accuracy of BDS3-derived ZTD is improved by 20.5% versus that of BDS2.  
72 Alcaay et al. (2021) compared the GPS-, GPS/GLONASS- and GPS/GLONASS/Galileo/BDS-PPP solutions



73 and found that the ZTD difference between the three schemes was less than 20 mm. Lu et al. (2017) compared  
74 the accuracy of the RT-PPP-derived ZTD using the different SSR products, and the multi-GNSS RT-PPP-  
75 derived ZTD based on GFZC2 SSR products showed the highest accuracy.

76 The ongoing discussion primarily centers on the influence of single- and multi-GNSS RT-PPP on the  
77 accuracy of RT ZTD. Yet, there is a limited discourse on the influence of the different ACs-based SSR  
78 corrections on the accuracy of RT ZTD. The quality of GNSS SSR products has improved with the increasing  
79 abundance of SSR products provided by IGS. Most studies have focused on BDS2 (Lu et al., 2015; Pan et  
80 al., 2018), while BDS3 needs to be sufficiently studied. Moreover, evaluating the influence of different GNSS  
81 SSR products for the accuracy of RT-PPP-derived ZTD is an important reference value for achieving high-  
82 precision and high-availability in RT-PPP-derived ZTD with the growth of SSR products. In this study,  
83 positioning performance and ZTD accuracy are estimated using the RT-PPP based on multi-GNSS from 8  
84 IGMAS stations from 355 in 2023 to 14 in 2024. Our primary objective is to compare the RT-PPP positioning  
85 performance, RT-PPP-derived ZTD accuracy and availability based on SSR products from different ACs.  
86 The findings serve as a valuable reference for selecting SSR products in RT-PPP-derived ZTD and hold  
87 significant importance for applications such as earth observation correction, meteorological disaster  
88 prediction, etc.

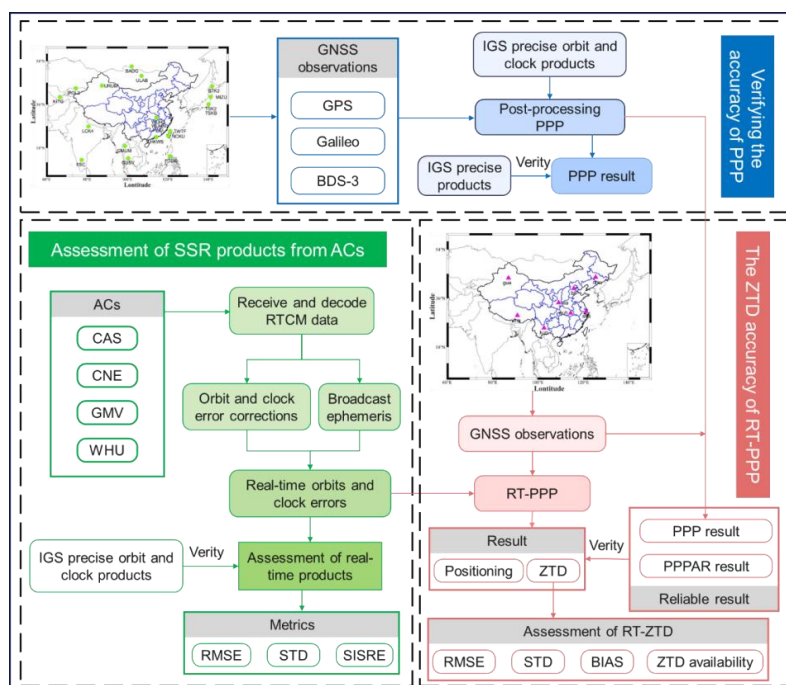
## 89 2 THE METHOD OF RT-PPP-DERIVED ZTD

### 90 2.1 Data collection

91 IGS was established to bolster geodetic and geodynamic research, officially launching its operations on  
92 January 1, 1994. IGS offers worldwide access to GNSS satellite observations from various tracking stations  
93 and products, including satellite ephemerides, clock errors, earth orientation parameters, atmospheres, etc.  
94 (Geng et al., 2021; Griffiths, 2019). IGMAS was established under the leadership of China in 2012. Its  
95 primary purpose is establishing an information platform equipped with data acquisition, storage, analysis,  
96 management, and release functions for the global RT tracking network of the four major satellite navigation  
97 systems with full arcs and multiple coverage observations. The leading indicators and operational status of  
98 GNSS were tested and assessed to generate products such as high-precision precision ephemerides, satellite  
99 clock errors, geotropic parameters, tracking station coordinates and rates, and global ionospheric delays(Li  
100 et al., 2022; Zhang et al., 2023).

101 The workflow of this study is shown in Figure 1 and includes three parts: verifying the performance of  
102 PPP, assessing different SSR products, and verifying the performance of RT-PPP using the results obtained  
103 by post-processing PPP and PRIDE PPPAR. In the first part, the position and ZTD are estimated using the  
104 multi-GNSS post-processing PPP technique from IGS stations in Asia-Pacific to verify the performance of  
105 multi-GNSS post-processing PPP. A total of 20 stations are selected in countries such as Mongolia, Russia,  
106 Japan, India, Thailand, and others. The 14 IGS sites with the highest availability are selected from the IGS  
107 sites for experimental analysis according to the number of observation documents. In the second part, the  
108 accuracies of SSR products from four ACs are evaluated. In the third part, the position and ZTD are estimated

109 using a multi-GNSS RT-PPP technique from 8 IGMAS stations in China. Data from DOY 355 in 2023 to  
 110 DOY 14 in 2024 are utilized. GPS, Galileo, and BDS3 can be received at these stations simultaneously. The  
 111 solutions obtained by PRIDE PPPAR and post-processing PPP are considered the reliable position and ZTD  
 112 to verify the performance of RT-PPP. Figure 2 displays the distribution information of the selected IGS and  
 113 IGMAS sites in this study and the information of IGMAS stations is shown in Table 1.

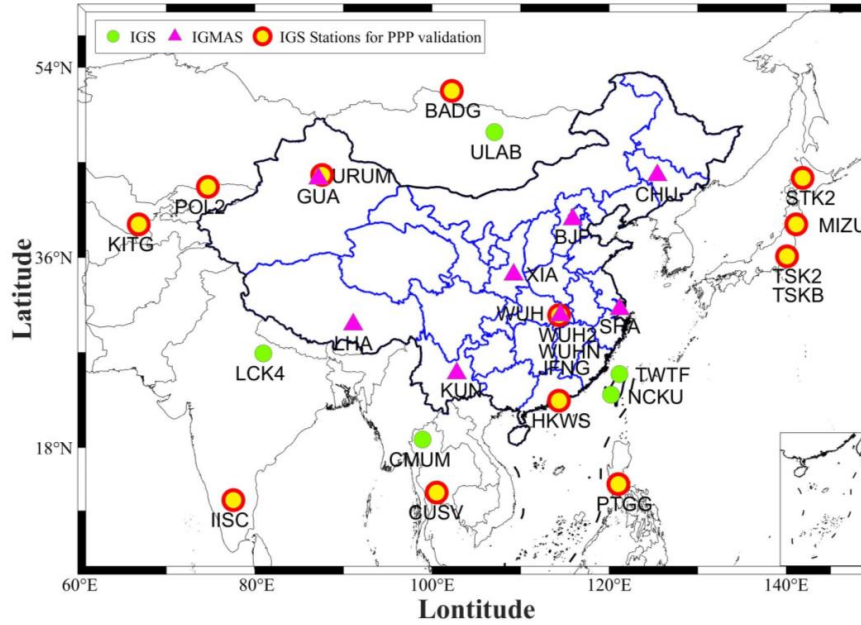


114  
 115  
 116

Figure 1. The workflow of this study.

Table 1. Location information of IGMAS stations.

Stations	Longitude/°	Latitude/°	Height/m	Geographical area
BJF	115.89	39.61	75.4	North China
CHU	125.44	43.79	273.9	Northeast Region
GUA	87.18	43.47	2029.3	Northwest China
KUN	102.80	25.03	1988.4	Southwest China
LHA	91.10	29.66	3630.2	Southwest China
SHA	121.20	31.10	20.9	East China
WUH	114.49	30.52	71.1	Central China
XIA	109.22	34.37	449.4	Northwest China



117

118

Figure 2. The distribution of IGMAS stations and IGS stations.

119 2.2 Recovering real-time products

120 IGS RT satellite orbit correction includes the position correction  $dO = [\delta O_r \ \delta O_a \ \delta O_c]^T$  and velocity  
 121 correction  $d\bar{O} = [\delta \bar{O}_r \ \delta \bar{O}_a \ \delta \bar{O}_c]^T$  at the reference moment; then the orbital correction at the moment  $t$   
 122 is:

123 
$$\delta O = O + d\bar{O}(t - t_0) \quad (1)$$

124 The orbital corrections from the spacecraft body-fixed system should be transformed to the Earth-Centered  
 125 Earth-Fixed (ECEF) system by means of a coordinate transformation. Since the positioning is usually done  
 126 in ECEF:

127 
$$X = \begin{bmatrix} \frac{\bar{r}}{|\bar{r}|} \times \frac{r \times \bar{r}}{|r \times \bar{r}|} & \frac{\bar{r}}{|\bar{r}|} & \frac{r \times \bar{r}}{|r \times \bar{r}|} \end{bmatrix} \delta O \quad (2)$$

128 where  $r = X_{brdc}$  refers to satellite positions from broadcast ephemeris.  $\bar{r} = \dot{X}_{brdc}$  refers to velocity from  
 129 broadcast ephemeris. The  $X_{pre}$  refers to precise satellite position, which can be calculated by:

130 
$$X_{pre} = X_{brdc} - \delta X \quad (3)$$

131 The RT correction of the clock error refers to the difference of precision clock error  $\delta t_{pre}$  versus broadcast  
 132 clock error  $\delta t_{brdc}$ , which is similar to RT orbital correction. However, the SSR clock error correction is  
 133 represented by  $c_0$ ,  $c_1$ , and  $c_2$  of the reference time  $t_0$  unlike orbital corrections and the RT correction  $\delta c$



134 is obtained by fitting  $c_0$ ,  $c_1$ , and  $c_2$ . The RT correction  $\delta c$  of the clock error at the moment  $t$  is:

$$135 \quad \delta c = c_0 + c_1(t - t_0) + c_2(t - t_0)^2 \quad (4)$$

136 Eventually, precision clock errors  $\delta t_{pre}$  were obtained by:

$$137 \quad \delta t_{pre} = \delta t_{brdc} - \delta c / C_{light} \quad (5)$$

138 where  $\delta t_{brdc}$  and  $C_{light}$  refers to clock error from broadcast ephemeris and speed of light.

### 139 2.3 PPP functional model

140 The impacts of satellite orbits and clock errors are mitigated by employing RT satellite orbits and clock  
 141 errors recovered by SSR in the PPP technique. ZTD is solved as an unknown parameter of the equation. The  
 142 principle is to construct two observation equations based on the ionosphere-free (IF) combinations of pseudo-  
 143 range and carrier phase observation (Ju et al., 2022; Ke et al., 2020). The basic observation equations can be  
 144 expressed as follows:

$$145 \quad \begin{cases} P_{r,i}^s = \rho_{r,i}^s + C_{light}(dt_r - dt^s) + I_{r,i}^s + T_r^s + b_{r,i} + b_{r,i}^s + \varepsilon_{r,p}^s \\ L_{r,i}^s = \rho_r^s + C_{light}(dt_r - dt^s) - I_{r,i}^s + T_r^s + \lambda_i N_{r,i}^s + \delta_{r,i} - \delta_{r,i}^s + \varepsilon_{r,\varphi}^s \end{cases} \quad (6)$$

146 where  $s$  refer to the satellites.  $r$  refer to the receiver. and  $i$  refer to the frequency.  $L_{r,j}^s$  and  $P_{r,j}^s$  are the  
 147 carrier phase and pseudo-range observation from receiver  $r$  to satellite  $S$ , respectively.  $\rho$  refers to the  
 148 satellite-receiver geometric distance.  $dt_r$  is the receiver clock error and  $dt^s$  is the satellite clock error.  $I$   
 149 is the Ionospheric delay.  $T_r^s$  refers to the tropospheric delay.  $\lambda$  is the wavelength.  $\delta$  and  $b$  denote the phase  
 150 delays and the code biases, respectively.  $N$  is the integer ambiguity.  $\varepsilon_{r,p}^s$  is the pseudo-range observation  
 151 noise.  $\varepsilon_{r,\varphi}^s$  is carrier phase observation noise.

152 The dual-frequency IF combination model is constructed and simplified from the equation(6):

$$153 \quad \begin{cases} P_{IF} = \rho - cdt + T_r^s + \varepsilon_{r,s}^s \\ L_{IF} = \rho - cdt + T_r^s + \lambda_1 N_{IF} + \varepsilon_{r,\varphi}^s \end{cases} \quad (7)$$

154 where  $L_{IF}$  is the carrier phase observation.  $P_{IF}$  is the pseudo-range observation. The unknown parameters  
 155 can be estimated in IF-PPP are as follows:

$$156 \quad X = \begin{bmatrix} x & \overline{cdt_r} & Z & \overline{N}_{IF}^s \end{bmatrix} \quad (8)$$

157 where  $x$  is the position of the receiver.  $\overline{cdt_r}$  refers to receiver clock error.  $Z$  refers to the Tropospheric  
 158 delay.  $\overline{N}_{IF}^s$  refers to the integer phase ambiguity.

### 159 2.4 Accuracy evaluation

160 Two methods were used to evaluate the accuracy of RT-PPP-derived ZTD at IGMAS stations. The first is  
 161 our post-processing PPP based on RTKLIP for secondary development, and the other one is PRIDE PPPAR



162 from Geng et al. of Wuhan University. The consistency between the solution data and the IGS precision  
 163 products is used to evaluate the positioning and ZTD accuracy of post-processing PPP for IGS stations. Gross  
 164 errors and outages in the RT clock error products will lead to an unreliable accuracy assessment of the RT  
 165 clock error products. The accuracy statistics of clock error may be affected if a single satellite's clock error  
 166 is used as the reference. Therefore, the average satellite clock error at the current epoch is used as a reference  
 167 to eliminate system errors in this study(Yao et al., 2017). The root mean square error (RMSE), standard  
 168 deviation (STD), and bias of the differences are used to evaluate SSR products and positioning and ZTD of  
 169 RT-PPP. The three metrics are calculated as follows(Su et al., 2023):

$$170 \quad \begin{cases} RMSE = \sqrt{\frac{1}{N} \sum_{i=1}^N \Delta^2} \\ STD = \sqrt{\frac{1}{N} \sum_{i=1}^N (\Delta - \Delta_{ave})^2} \\ BIAS = \frac{1}{N} \sum_{i=1}^N \Delta \end{cases} \quad (9)$$

171 where  $N$  is the sample number.  $\Delta$  is the difference of the SSR products versus the IGS precision products.  
 172  $\Delta_{ave}$  is the average  $\Delta$ .

173 The Pearson correlation coefficient (R) is also used to evaluate the consistency of reliable ZTD and RT-  
 174 PPP-derived ZTD. R is calculated as follows:

$$175 \quad R = \frac{\sum_{i=1}^N (ZTD_i^{der} - \overline{ZTD_i^{der}}) \sum_{i=1}^N (ZTD_i^{der} - \overline{ZTD_i^{ref}})}{\sqrt{\sum_{i=1}^N (ZTD_i^{der} - \overline{ZTD_i^{der}})^2 \sum_{i=1}^N (ZTD_i^{der} - \overline{ZTD_i^{ref}})^2}} \quad (10)$$

176 where  $ZTD_i^{der}$  is the PPP solution results;  $ZTD_i^{ref}$  refers to the tropospheric delay used as a reference.  
 177  $\overline{ZTD_i^{der}}$  and  $\overline{ZTD_i^{ref}}$  denote the mean of  $ZTD_i^{der}$  and  $ZTD_i^{ref}$  respectively.

$$178 \quad E_{SISRE} = \sqrt{[RMSE(\omega_R \Delta r_R - C_{light} \Delta C)]^2 + \omega_{A,C}^2 \{ [RMSE(\Delta r_A)]^2 + [RMSE(\Delta r_C)]^2 \}} \quad (11)$$

179 where  $E_{SISRE}$  refers to the SISRE;  $\Delta C$  is the difference of the RT clock error versus the IGS precision  
 180 products in each epoch;  $\Delta r_R$ ,  $\Delta r_A$ , and  $\Delta r_C$  are orbital errors in the radial, along-track, and cross-track (R/A/C)  
 181 direction in each epoch, respectively.  $\omega_R$  and  $\omega_{A,C}^2$  are weighting factors that convert the orbital errors in  
 182 the R/A/C direction to the orbital errors in the line-of-sight direction(Kazmierski et al., 2020). Different  
 183 Satellite systems have different SISRE weighting factors, as shown in Table 2.

184

Table 2 Weight factors of SISRE

Satellite system	$\omega_R$	$\omega_{A,C}^2$
GPS	0.98	1/49
Galileo	0.98	1/61
BDS (MEO)	0.98	1/54



BDS (IGSO, GEO)	0.99	1/126
-----------------	------	-------

185 3 ACCURACY EVALUATION OF SSR PRODUCTS

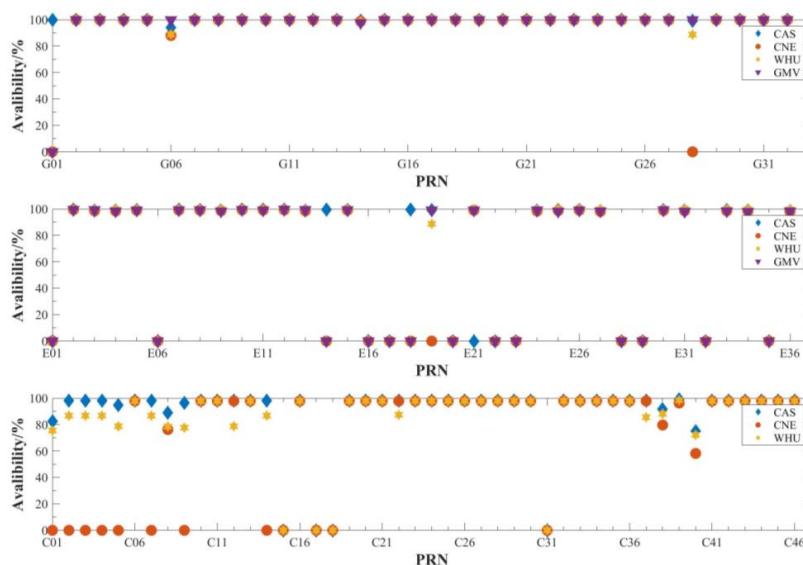
186 The stability of SSR streams can be influenced by various factors, including the receiving software,  
 187 network stability, and the broadcasting organization. In this study, RTKNAVI software is used to receive the  
 188 SSR products in the same network environment from the mount-points of SSRC00CAS0, SSRC00CNE0,  
 189 SSRC00GMV0, and SSRC00WHU0. The SSR product information for each subsystem center is shown in  
 190 Table 3.

191 Table 3. RTCM-SSR mount points Description.

ACs	Name of Institutions	Mount-points	Supported systems	Update Interval of Orbit/s	Update Interval of Clock/s	Reference Point
CAS	Chinese Academy of Sciences	SSRC00CAS0	GPS+GLO+GAL+BDS	5	5	CoM
CNE	Centre National d'Etudes Spatiales	SSRC00CNE0	GPS+GLO+GAL+BDS	5	5	CoM
GMV	GMV Aerospace and Defense	SSRC00GMV0	GPS+GLO+GAL+BDS	5	5	CoM
WHU	Wuhan University	SSRC00WHU0	GPS+GLO+GAL+BDS	5	5	CoM

192 3.1 SSR Products availability

193 The SSR product completeness rates for the four ACs were assessed for 26 days, from DOY 355 in 2023  
 194 to 14 in 2024, as illustrated in Figure 3. Notably, the study excluded the unhealthy satellite G01 from  
 195 consideration. Since SSR corrections for 31 GPS satellites, 24 Galileo satellites, and 27 BDS3 satellites can  
 196 be obtained, CAS has the higher satellite availability. WHU offers SSR corrections for 31 GPS satellites, 23  
 197 Galileo satellites, and 27 BDS3 satellites. CNE demonstrates lower availability, providing 30 GPS satellites,  
 198 22 Galileo satellites, and 27 BDS3 satellites. GMV provides SSR corrections for 31 GPS satellites and 23  
 199 Galileo satellites. BDS-SSR products obtained by GMV are unavailable due to software decoding issues with  
 200 GMV-SSR products during the experimental data period of this study, which resulted in pseudo-random  
 201 noise and issue of data ephemeris errors for its BDS satellites. Although the variation of epoch availability  
 202 for GPS, Galileo, and BDS3 SSR corrections from different ACs is different, the average epoch availability  
 203 of the SSR products provided by the four ACs is above 97.5%.



204

205

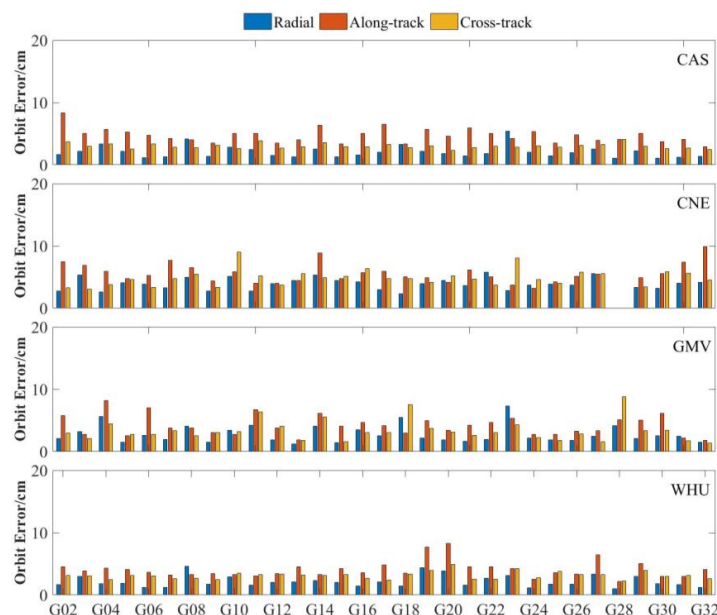
Figure 3. Epoch availability of SSR corrections during the experiment.

206

### 3.2 Accuracy of SSR products

207

IGS precision products were chosen as references to evaluate different SSR products. The RMSEs of GPS  
208 RT orbits in the R/A/C directions for the four ACs are shown in Figure 4. The average RMSEs of GPS,  
209 Galileo, and BDS3 RT orbits in the R/A/C directions are shown in Table 4. Figure 4 and Table 4 show that  
210 the RMSEs of orbit products in the R-direction are mostly smaller than in the C-direction, with the RMSEs  
211 of orbit products in the R-direction being the largest due to the observation being mainly centered around the  
212 R-direction. The accuracies of GPS, Galileo, and BDS3 RT orbits from different ACs are individually  
213 evaluated. The accuracies of GPS RT orbits from four ACs reach the centimeter level and WHU has the best  
214 accuracy, followed by CAS and GMV. GPS RT orbits from CNE are relatively worse, with 8.09 cm. Galileo  
215 RT orbits from CAS exhibit the lowest error, followed by WHU and GMV, with CNE showing relatively  
216 worse accuracy with 10.28 cm. The accuracies of BDS3 RT orbits from four ACs are better than 17 cm. The  
217 accuracy of BDS3 RT orbits from WHU is the best, CAS is the second with 14.18 cm, and the products from  
218 CNE are worse, with 16.42 cm. Overall, Galileo RT orbits from CAS display the best accuracy, with 5.91  
219 cm, while WHU has the best accuracies of GPS and BDS3 RT orbits, with 5.57 cm and 11.77 cm, respectively.



220

221

222

Figure 4. The RMSE values in R/A/C directions of GPS RT orbit from different ACs.

Table 4. The mean accuracies of GPS, Galileo, and BDS3 RT precise products from different ACs/cm.

		R	A	C	3D						
CAS	GPS	2.07	4.68	3.08	5.97	CNE	GPS	3.82	5.28	4.80	8.09
	GAL	1.91	4.67	3.09	5.91		GAL	6.92	5.70	5.02	10.28
	BDS3	6.67	10.32	7.08	14.18		BDS3	5.50	12.57	9.02	16.42
GMV	GPS	2.82	4.40	3.54	6.31	WHU	GPS	2.20	4.06	3.13	5.57
	GAL	2.18	6.59	3.61	7.82		GAL	2.73	5.31	4.20	7.30
-	-	-	-	-	-		BDS3	5.30	8.41	6.31	11.77

223

224

225

226

227

228

229

230

231

Figure 5 displays the RMSEs and STDs of GPS RT clock errors from four ACs. Table 5 shows the RMSEs and STDs of GPS, Galileo, and BDS3 RT clock errors. The RT clock errors of G03 provided by CNE and WHU are excluded from this study due to their gross errors. The remaining GPS satellites are used commonly. The mean STDs of GPS RT clock errors from CAS, GMV, and CNE are 0.16, 0.19, and 0.14 ns, respectively, with the largest STD from WHU being 0.22 ns. For Galileo, CAS RT clock errors display the best accuracy, with a mean STD of 0.11 ns. For BDS3, WHU RT clock errors have the best accuracy with STD of 0.39 ns. Overall, the mean STDs of GPS, Galileo, and BDS3 from the three ACs are better than 0.22, 0.19, and 0.55 ns, respectively, and the mean RMSEs of GPS, Galileo, and BDS3 from these ACs are better than 0.54, 0.32, and 1.46 ns, respectively.



Figure 5. The RMSEs and STDs of GPS RT clock errors from different ACs.

232  
 233  
 234

Table 5. The mean accuracies of GPS, Galileo, and BDS3 RT precise products from different ACs/cm.

		RMSE		STD				RMSE		STD	
CAS	GPS	0.38	0.16	CNE	GPS	0.41	0.19				
	GAL	0.17	0.11		GAL	0.32	0.17				
	BDS3	1.03	0.41		BDS3	1.76	0.84				
GMV	GPS	0.38	0.14	WHU	GPS	0.54	0.22				
	GAL	0.21	0.19		GAL	0.24	0.14				
-	-	-	-	BDS3	1.02	0.39					

235 3.3 Accuracy of SISRE

236 Table 6 shows the average SISREs of GPS, Galileo, and BDS3 from four ACs. For GPS, the order of  
 237 magnitude of SISREs for different ACs is WHU>CNE>GMV>CAS. For Galileo, CAS and WHU have the  
 238 better SISRE with around 5 cm and CNE has the worst SISRE with 9.80 cm. For BDS3, the SISREs of CAS  
 239 and WHU are significantly better than the SISRE of CNE, which are 29.11, 29.98, and 57.48 cm, respectively.  
 240 Overall, CAS has the best SISREs of GPS, Galileo, and BDS3, followed by WHU as the second, while CNE  
 241 and GMV exhibit the worst accuracy.

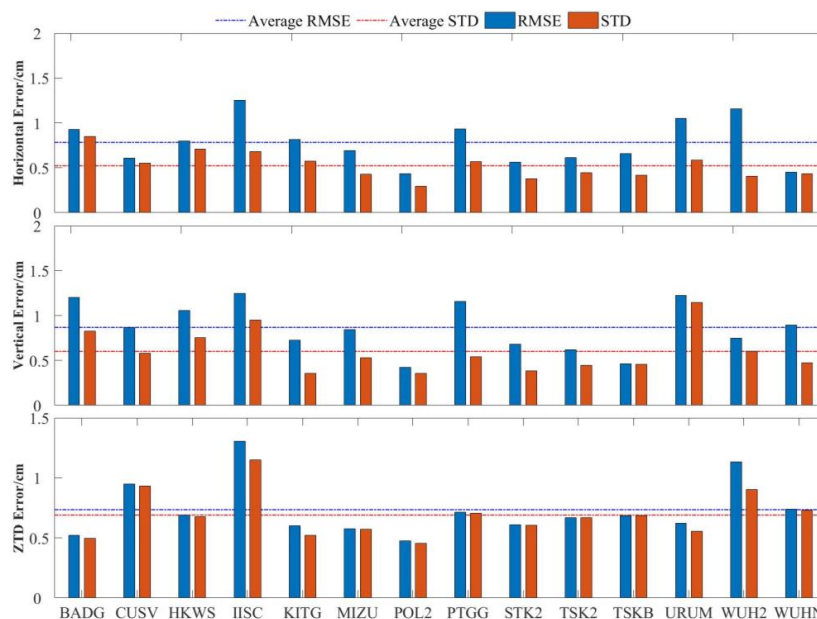
242 Table 6. Mean SISRE of GPS, BDS, and BDS3 satellite of SSR products from different ACs/cm.

		SISRE		SISRE	
CAS	GPS	9.50	CNE	GPS	11.06
	GAL	4.91		GAL	9.80
	BDS3	29.11		BDS3	57.48
GMV	GPS	10.44	WHU	GPS	12.55
	GAL	6.64		GAL	4.93

243 4 RESULT

244 4.1 Performances of multi-GNSS PPP at IGS stations

245 IGS post-processed precise position and ZTD products were used to evaluate the multi-GNSS post-  
246 processing PPP performance at 14 IGS sites in and around China. The average convergence time of all  
247 stations are less than 20 minutes. The station coordinates from the IGS SINEX files and the ZTD from the  
248 IGS ZPD files were used as references. Positioning performance and ZTD accuracy of post-processing PPP  
249 are shown in Figure 6. The RMSEs of horizontal (H-D) and vertical (V-D) errors are within 15 mm for all  
250 sites, respectively. The RMSEs of ZTD are within 10 mm for most sites, with an average RMSE of 7.4 mm.  
251 The abovementioned results suggest that post-processing PPP demonstrates good performance in both  
252 positioning and ZTD and can be used to verify the performance of RT-PPP.



253

254 Figure 6. RMSEs and STDs of the positioning performance and ZTD accuracy of post-processing PPP,  
255 respectively.

256 4.2 RT-PPP with SSR products from different ACs in the IGMAS station

257 4.2.1 Convergence time of RT-PPP

258 To assess the accuracy of four SSR products, the eight IGMAS stations were selected for RT-PPP after  
259 verifying the performance of post-processing PPP. The testing period spans from DOY 355 in 2023 to DOY  
260 14 in 2024. The LHA is excluded due to a low number of observations among the eight IGMAS stations. The  
261 IF model was used. The parameter estimation method was the Kalman filter, and additional positioning  
262 strategies were presented in Table 7.

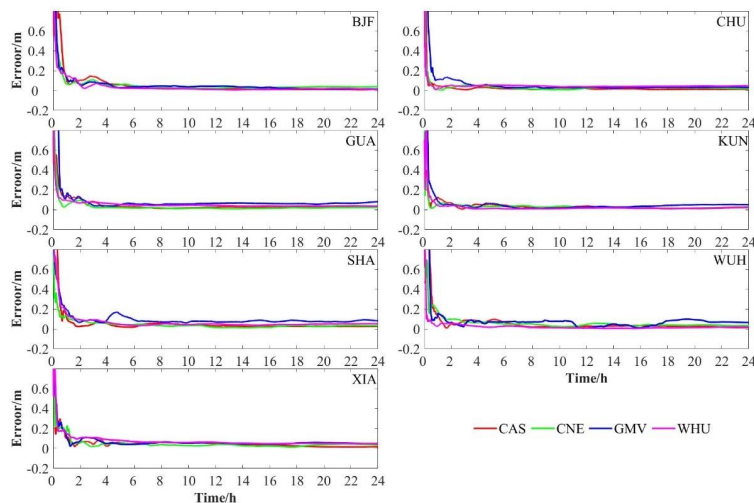
263

Table 7. Strategies for RT-PPP.

Items	Correction model or estimation strategy
Estimator	Kalman filter
Observations	IF code and phase combinations
Sampling rate	30 s
Cut-off elevation	10°
Phase-windup effect	Corrected
Tropospheric delay	Saastamoinen
Ionospheric delay	Estimated as a random-walk noise process
Relativistic effects	Eliminated by IF combination
antenna phase center	Corrected
Orbit and clock product	igs14.atx
Phase ambiguities	SSR corrections + broadcast ephemeris
	Float

264

265 The convergence time, positioning, and ZTD accuracies for multi-GNSS RT-PPP were assessed based on  
 266 the different SSR products. The convergence time is the initial epoch where the error of H-D and V-D  
 267 direction are both less than 10 cm, holding for 20 epochs. Figure 7 shows multi-GNSS RT-PPP positioning  
 268 errors in the 3D direction using the SSR products from the four ACs at seven stations on DOY 12, 2024. The  
 269 results of RT-PPP from different ACs are represented by distinct colors, respectively, and the seven sub-  
 270 figures represent the seven IGMAS sites, respectively. The sub-figures are set with the same range of V-D  
 271 axes for comparison and the X direction is the hour since the start of the solution. The average convergence  
 272 time of four ACs is less than 30 min, and the 3D positioning accuracies of four ACs are better than 10 cm  
 273 after completing the convergence process.



274

275

Figure 7. RT-PPP errors of different ACs at seven IGMAS stations.

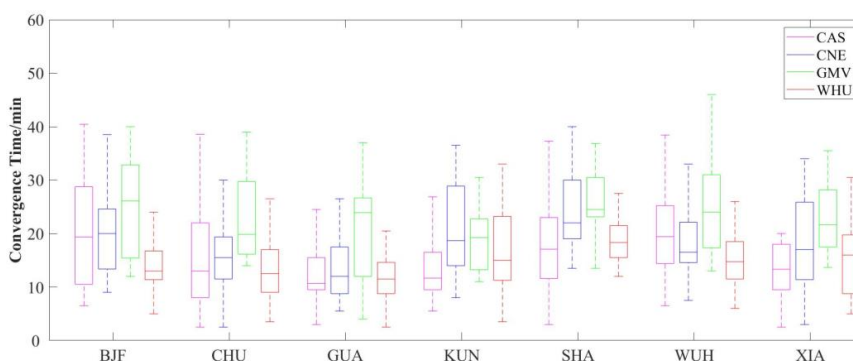
276

277

278

The convergence time for seven stations over 26 days from four ACs was counted. Figure 8 shows box plots of the convergence time, including the median, 25% quantile, and 75% convergence time. Table 8 provides a detailed breakdown of convergence time statistics for four ACs. The average convergence time at

279 all sites based on CAS, WHU, and CNE is less than 20 min, while GMV is 22.8 min. The discrepancy in the  
 280 convergence time from GMV and other ACs may be because that RT-PPP based on GMV-SSR products  
 281 only uses GPS and Galileo, with fewer satellites than the other analysis centers. The average convergence  
 282 time for CAS and WHU are similar with 14.9 min and 14.4 min, respectively, and for CNE is 17.4 min, which  
 283 is slightly longer than CAS and WHU because CNE has fewer satellites available than CAS and WHU.



284

Figure 8. Boxplot of the convergence time of different ACs at IGMAS stations.

285

286

Table 8. The MAX, MIN, and MEAN of the convergence time derived from RT-PPP of different ACs/min.

ACs	Stations	MAX	MIN	MEAN	Stations	MAX	MIN	MEAN
CAS	BJF	40.0	6.5	19.4	CHU	45.0	3.0	13.0
	GUA	31.0	3.0	10.7	KUN	45.0	5.5	11.7
	SHA	43.5	3.5	17.1	WUH	35.0	6.5	19.4
	XIA	40.5	5.0	13.3	-	-	-	-
CNE	BJF	39.5	6.0	20.0	CHU	26.0	3.0	15.5
	GUA	25.5	3.5	12.0	KUN	46.0	6.5	18.7
	SHA	38.0	15.5	22.0	WUH	39.5	6.0	16.5
	XIA	31.0	3.0	17.0	-	-	-	-
GMV	BJF	40.0	12.0	26.1	CHU	39.0	14.0	19.8
	GUA	37.0	5.0	23.9	KUN	30.5	11.0	19.3
	SHA	36.0	13.5	24.5	WUH	46.0	13.0	24.0
	XIA	35.5	14.0	21.7	-	-	-	-
WHU	BJF	24.0	5.0	13.0	CHU	26.5	3.5	12.5
	GUA	20.5	3.0	11.5	KUN	33.0	3.5	15.0
	SHA	27.5	11.0	18.3	WUH	26.0	6.0	14.8
	XIA	30.5	5.0	16.0	-	-	-	-

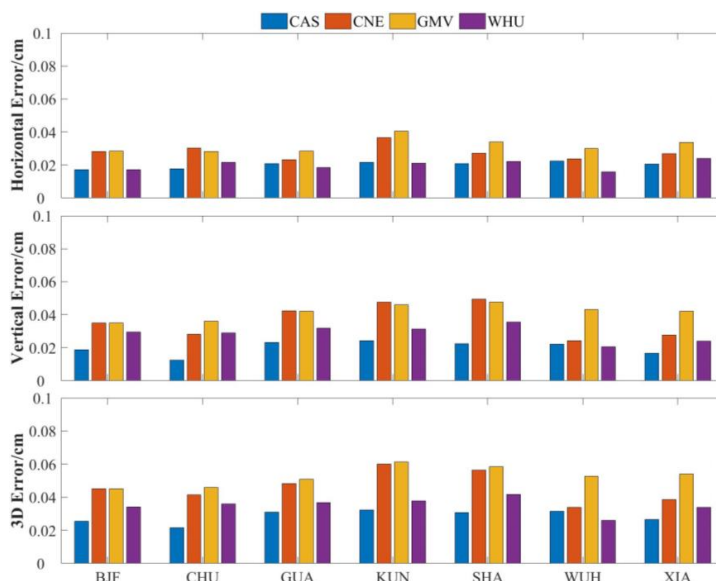
287

#### 4.2.2 Positioning accuracy of RT-PPP

288

The positioning accuracies of RT-PPP for each AC at the seven IGMAS stations were evaluated. Figure 9  
 289 shows the positioning accuracies in H-D, V-D, and 3D directions. CAS exhibits the highest accuracy, with  
 290 2.1, 2.4, and 3.2 cm in three aspects, respectively. Then, WHU shows a 3.3 cm accuracy in the 3D direction,  
 291 which is similar to the positioning accuracy of CAS. Since the RMSEs of the SSR products from CNE are  
 292 higher than those of CAS and WHU, the PPP-performance based on CNE is unsatisfactory than CAS and  
 293 WHU. The positioning accuracy with GMV is the worst compared with other ACs. The positioning  
 294 performances of RT-PPP based on GMV-SSR products are 3.2 cm in H-D directions and 4.2 cm in V-D  
 295 directions. The mean RMSE of 3D positioning accuracy exceeds 5 cm, which is all higher than those of the

296 remaining three ACs. Therefore, the combination with BeiDou satellite can improve the positioning  
297 performance of RT-PPP.



298

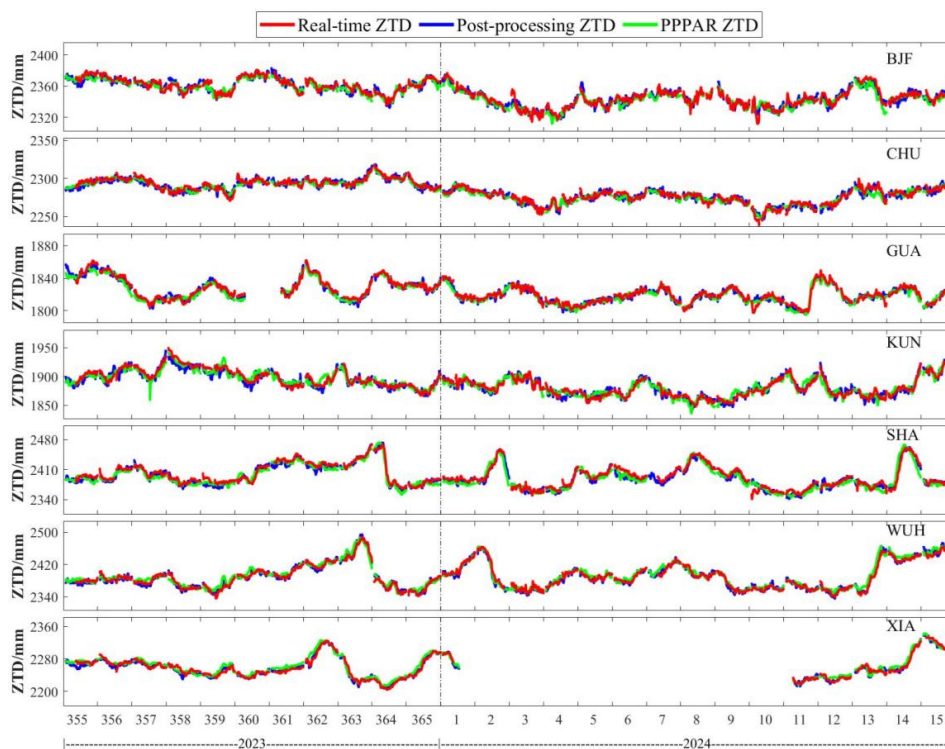
299 Figure 9. The positioning accuracies in H-D, V-D, and 3D directions of different ACs at seven IGMAS  
300 stations.

### 301 4.3 Accuracy of RT-PPP-derived ZTD

#### 302 4.3.1 Accuracy of RT-PPP-derived ZTDs obtained by different SSR products

303 RT-PPP-derived ZTDs based on four AC SSR products were compared with post-processing PPP and  
304 PRIDE PPPAR-derived ZTDs, respectively, to verify the accuracy of RT-PPP ZTD retrieval. Figure 10  
305 shows timing diagrams for RT-PPP-derived ZTDs obtained by WHU-SSR products alongside those of  
306 PRIDE PPPAR and post-processing PPP-derived ZTDs. RT-PPP, post-processing PPP, and PRIDE PPPAR-  
307 derived ZTDs have a similar trend. Table 9 shows the differences of RT-PPP-derived ZTDs versus PRIDE  
308 PPPAR-derived ZTDs for each AC at the seven IGMAS stations. The GUA station lacked observation data  
309 from 7:00 AM on DOY 360 to 7:00 AM on DOY 361 in 2023. And the XIA station lacked observation data  
310 from 1:00 PM on DOY 1 to 5:00 AM on DOY 11 in 2024. RT-PPP-derived ZTDs accuracies for GMV can  
311 be reached centimeter level. Furthermore, the average accuracies of RT-PPP-derived ZTDs for CAS, WHU,  
312 and CNE reach the millimeter level. RT-PPP-derived ZTDs based on WHU have the highest ZTD accuracy  
313 with an RMSE of 6.06 mm. CAS and WHU exhibit similar ZTD accuracies with 6.80 mm. The accuracy of  
314 RT-PPP-derived ZTDs based on GMV-SSR products is the worst, with 10.30 mm. The accuracy of RT-PPP-  
315 derived ZTDs based on GMV is worse than the other ACs, probably because GMV does not provide BDS3  
316 SSR products. The STDs of each AC are similar to the RMSEs, with WHU being the best, CAS being slightly  
317 inferior, and GMV being the worst. The bias of four ACs exhibits minimal differences with around 2.30 mm.  
318 The average R of four ACs exceed 0.9, with 0.96/0.93/0.93/0.97, respectively, indicating that RT-PPP-

319 derived ZTD strongly correlates with PRIDE PPPAR-derived ZTD. The result of RT-PPP-derived ZTD  
 320 versus post-processing PPP-derived ZTD is similar. The order of RMSEs and STDs for different ACs is  
 321 GMV>CNE>CAS>WHU. The average R of four ACs also exceed 0.9 with 0.96/0.95/0.91/0.97, respectively.  
 322 In summary, the accuracy of RT-PPP ZTD retrieval obtained by WHU-SSR products is the best.



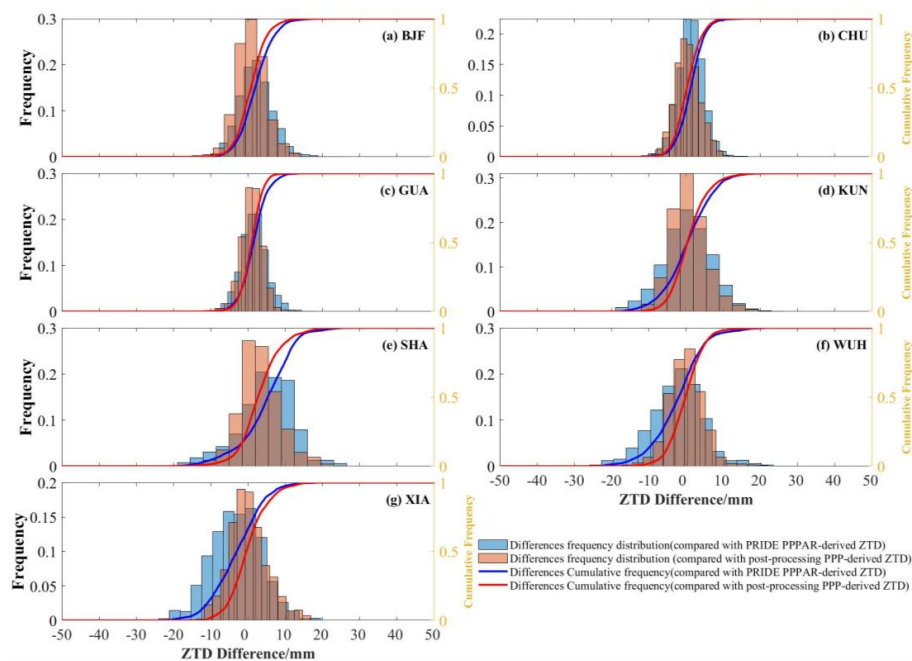
323  
 324 Figure 10. RT-PPP, post-processing PPP, and PRIDE PPPAR-derived ZTDs at IGMAS stations.

325 Table 9. The accuracies of RT-PPP-derived ZTDs from different ACs at seven IGMAS stations/mm.

AC	Stations	RMSE	STD	Bias	R	AC	Stations	RMSE	STD	Bias	R
CAS	BJF	7.01	6.57	2.44	0.94	CNE	BJF	7.92	7.04	3.62	0.92
	CHU	3.25	3.21	0.49	0.98		CHU	5.04	4.75	1.68	0.95
	GUA	4.01	3.49	1.97	0.98		GUA	5.62	5.57	0.73	0.93
	KUN	7.23	7.08	-1.47	0.97		KUN	9.73	9.17	3.26	0.91
	SHA	9.2	7.14	5.8	0.94		SHA	13.03	11.1	6.82	0.93
	WUH	9.96	8.65	-4.95	0.97		WUH	11	10.38	-3.65	0.96
	XIA	7	5.99	3.61	0.98		XIA	8.02	7.83	1.71	0.97
Mean	6.80	6.01	1.12	0.96	Mean	8.62	7.97	2.02	0.93		
GMV	BJF	10	10	0.27	0.91	WHU	BJF	4.98	4.46	2.21	0.96
	CHU	6.75	6.19	2.69	0.96		CHU	3.58	3.35	1.26	0.98
	GUA	8.09	6.7	4.53	0.95		GUA	3.79	3.45	1.57	0.97
	KUN	9.12	9	1.46	0.91		KUN	6.4	6.38	0.51	0.95
	SHA	13.47	11.03	7.73	0.94		SHA	8.94	7.49	4.91	0.97
	WUH	12.78	12.69	-1.47	0.95		WUH	7.42	7.01	-2.42	0.98
	XIA	11.95	11.93	0.61	0.94		XIA	7.33	6.68	3.02	0.98
Mean	10.30	9.64	2.26	0.93	Mean	6.06	5.54	1.58	0.97		

326

327 The differences of RT-PPP-derived ZTD versus PRIDE PPPAR and post-processing PPP-derived ZTD  
328 were counted separately to further analyze the ZTD consistency, respectively. Figure 11 shows the  
329 differences distribution of RT-PPP compared with PRIDE PPPAR and post-processing PPP-derived ZTDs,  
330 respectively, where the bar graph shows the differences frequency distribution and the curve shows the  
331 differences cumulative frequency. The differences frequency of RT-PPP-derived ZTDs versus PRIDE  
332 PPPAR and post-processing PPP-derived ZTDs at the seven stations are normally distributed, respectively.  
333 The bias of RT-PPP-derived ZTDs at all stations is nearly 0 mm. The differences distribution of RT-PPP-  
334 derived ZTDs based on the other ACs were also counted, and the bias was nearly 0 mm. The measure of  
335 dispersion of RT-PPP-derived ZTDs based on WHU is lower than CAS, GMV, . Therefore, RT-PPP-derived  
336 ZTDs based WHU SSR products have the best ZTD retrieval accuracy. The result is consistent with the  
337 conclusion of 3.2.1.



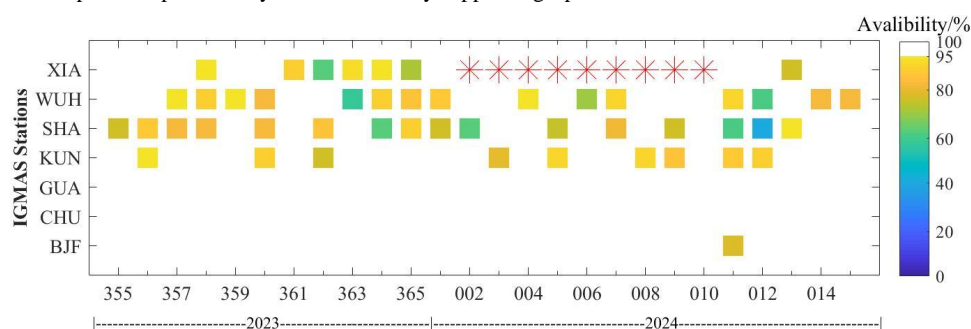
338

339 Figure 11. The differences distribution of RT-PPP-derived ZTDs compared with post-processing PPP and  
340 PRIDE PPPAR-derived ZTDs.

#### 341 4.3.2 RT-ZTD availability

342 The availability of RT-PPP-derived ZTD was assessed. RT-PPP-derived ZTD in the epoch is considered  
343 unavailable if the differences of RT-PPP-derived ZTD versus PRIDE PPPAR and post-processing PPP-  
344 derived ZTD in arbitrary epoch are more than 10 mm, respectively. The daily availability of RT-PPP-derived  
345 ZTD based on WHU-SSR products was calculated (Figure 12). Daily ZTD availability of sites with less ZTD  
346 variations can be maintained at more than 95%, such as BJF, CHU, and GUA. Daily ZTD availability of sites  
347 with large ZTD variations can basically be maintained at more than 80%. A similar result also appears in the

348 comparison between RT-PPP-derived ZTD and post-processing PPP-derived ZTD. Table 10 shows the  
 349 availability of RT-PPP-derived ZTD for the four SSR products at the seven stations using PRIDE PPPAR-  
 350 derived ZTD as references. RT-PPP-derived ZTDs based on WHU-SSR products have the highest  
 351 availability, with an average availability of 89% at all stations. The ZTD availability of CAS is slightly lower  
 352 with 85% and CNE is lower than CAS and WHU with 78%. GMV shows the worst availability with 70%.  
 353 The ZTD availability is positively correlated with the SISRE of SSR products from different ACs. Therefore,  
 354 the SSR products provided by WHU effectively support high-precision RT-PPP ZTD retrieval.



355  
 356 Figure 12. The availability of RT-PPP-derived ZTDs from WHU SSR products at seven IGMAS  
 357 stations/mm.

358 Table 10. The availability of RT-PPP-derived ZTDs from different AC products at IGMAS stations/%.

ACs	BJF	CHU	GUA	KUN	SHA	WUH	XIA	sum
CAS	91	99	97	83	74	72	79	85
CNE	83	95	92	71	57	69	80	78
GMV	75	87	80	77	51	58	62	70
WHU	97	99	98	90	77	85	82	89

359 5 CONCLUSIONS

360 Evaluating the accuracies of RT-PPP-derived ZTD based on SSR products from different ACs is crucial  
 361 in warning and forecasting extreme natural disasters and earth observation error correction. In this study, the  
 362 accuracies of GPS, Galileo, and BDS3 RT satellite orbit and clock error products from four ACs were  
 363 evaluated. Then the positioning performance and ZTD accuracies for multi-GNSS RT-PPP were assessed.  
 364 The following conclusions were obtained. The average epoch availability of SSR corrections provided by  
 365 four ACs exceeds 97.5%, and CAS-SSR products have the highest satellite availability. CAS has the best  
 366 SISREs of GPS, Galileo, and BDS3, followed by WHU, while CNE and GMV exhibit the worst performance.  
 367 The results of multi-GNSS RT-PPP indicate that WHU achieves the shortest average convergence times with  
 368 14.4 min, followed by CAS and CNE. The average convergence time of GMV is 22.8 min, significantly  
 369 lower than other ACs. The accuracies of RT-PPP-derived ZTD obtained by four ACs are better than 11 mm,  
 370 and RT-PPP-derived ZTD is in good conformity with PRIDE PPPAR-derived ZTD. Among the four ACs,  
 371 WHU has the best accuracy of RT-PPP-derived ZTD with an average RMSE of 6.1 mm, and RT-PPP-derived



372 ZTD based on WHU SSR products has the highest availability with 89%. This study is essential for selecting  
373 SSR products from different ACs for RT-PPP ZTD retrieval.

374

375

376 Data availability

377 The IGMAS GNSS data are available from Wuhan University, but restrictions apply to the availability of  
378 these data, which were used under licence for the current study and so are not publicly available. The data  
379 are, however, available from the authors upon reasonable request and with the permission of Wuhan  
380 University. Post-processing products and GNSS data from IGS are available at  
381 <https://cddis.nasa.gov/archive/gnss/>. Post-processing products and GNSS data from IGS are available at  
382 [ntrip.gnsslab.cn](http://ntrip.gnsslab.cn).

383

384 Author contributions

385 WQY and HRH provided the initial idea and designed the experiments for this study; QZ guided the entire  
386 process of this study; XWM and QZ analyzed the data and wrote the manuscript; YBY, XHL, QZZ and YZH  
387 helped with the writing. All authors reviewed the manuscript.

388

389 Competing interests

390 The authors declare that they have no known competing financial interests or personal relationships that  
391 could have influenced the work reported in this paper.

392

393 Disclaimer

394 Publisher's note: Copernicus Publications remains neutral with regard to jurisdictional claims made in  
395 the text, published maps, institutional affiliations, or any other geographical representation in this paper.  
396 While Copernicus Publications makes every effort to include appropriate place names, the final  
397 responsibility lies with the authors.

398

399 Acknowledgments

400 The reviewers' and editors' comments are highly appreciated. We thank IGMAS and IGS for providing  
401 GNSS data for this analysis. We also thank IGS for providing the SSR products and precision products.

402

403 Funding

404 This work was supported by the State Key Laboratory of Geodesy and Earth's Dynamics, Innovation  
405 Academy for Precision Measurement Science and Technology, Chinese Academy of Sciences  
406 (SKLGED2024-3-8), the National Natural Science Foundation of China (42330105), the National Natural  
407 Science Foundation of China (42201484), also in part by Key Laboratory of Mine Geological Hazards  
408 Mechanism and Control, Ministry of Natural Resources (6000230168), and China Postdoctoral Science



409 Foundation (2023MD744243).

410

411 Author details

412 <sup>1</sup>Wanqiang Yao, Haoran Huang, Xiongwei Ma, Xiaohu Lin, Qingzhi Zhao, Yunzheng Huang are with the  
413 College of Geomatics, Xi'an University of Science and Technology, Xi'an 710054, China, (e-mail:  
414 sxywq@163.com; huanghr0213@163.com; xiongw\_ma@xust.edu.cn; xhlin214@xust.edu.cn;  
415 zhaoqingzhia@163.com; huangyunzheng0527@163.com).

416 <sup>2</sup>Qi Zhang, Yibin Yao are with the School of Geodesy and Geomatics, Wuhan University. Wuhan 430000,  
417 China. (e-mail: qizhangsgg@whu.edu.cn; ybyao@whu.edu.cn).

418

419 References

420 Alcay, S., and Turgut, M.: Evaluation of the positioning performance of multi-GNSS RT-PPP method, Arab.  
421 J. Geosci., 14, 1-19, <https://doi.org/10.1007/s12517-021-06534-4>, 2021.

422 Capilla, R. M., Berné, J. L., Martín, A., and Rodrigo, R.: Simulation case study of deformations and landslides  
423 using real-time GNSS precise point positioning technique, Geomat. Nat. Haz. Risk., 7, 1856-1873,  
424 <https://doi.org/10.1080/19475705.2015.1137243>, 2016.

425 Crocetti, L., Schartner, M., Zus, F., Zhang, W., Moeller, G., Navarro, V., See, L., Schindler, K., and Soja, B.:  
426 Global, spatially explicit modelling of zenith wet delay with XGBoost, J. Geodesy., 98, 23,  
427 <https://doi.org/10.1007/s00190-024-01829-2>, 2024.

428 Edokossi, K., Calabria, A., Jin, S., and Molina, I.: GNSS-reflectometry and remote sensing of soil moisture:  
429 A review of measurement techniques, methods, and applications, Remote Sensing, 12, 614,  
430 <https://doi.org/10.3390/rs12040614>, 2020.

431 Elsobey, M., and Al-Harbi, S.: Performance of real-time Precise Point Positioning using IGS real-time  
432 service, GPS solutions, 20, 565-571, <https://doi.org/10.1007/s10291-015-0467-z>, 2016.

433 Eugenia Bianchi, C., Oscar Mendoza, L. P., Isabel Fernandez, L., Paula Natali, M., Margarita Meza, A., and  
434 Francisco Moirano, J.: Multi-year GNSS monitoring of atmospheric IWV over Central and South  
435 America for climate studies, Ann. Geophys., 34, 623-639, [https://doi.org/10.5194/angeo-34-623-](https://doi.org/10.5194/angeo-34-623-2016)  
436 2016, 2016.

437 Gao, M., Xu, C., and Liu, Y.: Evaluation of Time-Series InSAR Tropospheric Delay Correction Methods  
438 over Northwestern Margin of the Qinghai-Tibet Plateau, Geomatics and Information Science of  
439 Wuhan University, 46, 1548-1559, <https://doi.org/10.1016/j.scitotenv.2024.170875>, 2021.

440 Ge, Y., Chen, S., Wu, T., Fan, C., Qin, W., Zhou, F., and Yang, X.: An analysis of BDS-3 real-time PPP:  
441 Time transfer, positioning, and tropospheric delay retrieval, Measurement, 172, 108871,  
442 <https://doi.org/10.1016/j.measurement.2020.108871>, 2021.

443 Geng, J., Yang, S., and Guo, J.: Assessing IGS GPS/Galileo/BDS-2/BDS-3 phase bias products with PRIDE  
444 PPP-AR, Satellite Navigation, 2, 1-15, <https://doi.org/10.1186/s43020-021-00049-9>, 2021.

445 Griffiths, J.: Combined orbits and clocks from IGS second reprocessing, J. Geodesy., 93, 177-195,  
446 <https://doi.org/10.1007/s00190-018-1149-8>, 2019.



- 447 Gu, S., Guo, R., Gong, X., Zhang, S., Lou, Y., and Li, Z.: Real-time precise point positioning based on BDS-  
448 3 global short message communication, *GPS Solutions*, 26, 107, [https://doi.org/10.1007/s10291-](https://doi.org/10.1007/s10291-022-01291-7)  
449 022-01291-7, 2022.
- 450 Hadas, T., Hobiger, T., and Hordyniec, P.: Considering different recent advancements in GNSS on real-time  
451 zenith troposphere estimates, *GPS Solutions*, 24, 99, <https://doi.org/10.1007/s10291-020-01014-w>,  
452 2020.
- 453 He, L., Yao, Y., Xu, C., Zhang, H., Tang, F., Ji, C., Liu, Z., and Wu, W.: A New Global ZTD Forecast Model  
454 Based on Improved LSTM Neural Network, *IEEE. J-STARS.*,  
455 <https://doi.org/10.1109/JSTARS.2024.3391821>, 2024.
- 456 Jiao, G., Song, S., Ge, Y., Su, K., and Liu, Y.: Assessment of BeiDou-3 and multi-GNSS precise point  
457 positioning performance, *Sensors*, 19, 2496, <https://doi.org/10.3390/s19112496>, 2019.
- 458 Ju, B., Jiang, W., Tao, J., Hu, J., Xi, R., Ma, J., and Liu, J.: Performance evaluation of GNSS kinematic PPP  
459 and PPP-IAR in structural health monitoring of bridge: Case studies, *Measurement*, 203, 112011,  
460 <https://doi.org/10.1016/j.measurement.2022.112011>, 2022.
- 461 Kazmierski, K., Zajdel, R., and Sońnica, K.: Evolution of orbit and clock quality for real-time multi-GNSS  
462 solutions, *GPS solutions*, 24, 111, <https://doi.org/10.1007/s10291-020-01026-6>, 2020.
- 463 Ke, S., and Shuanggen, J.: Analysis and comparisons of the BDS/Galileo quad-frequency PPP models  
464 performances, *Acta Geodaetica et Cartographica Sinica*, 49, 1189,  
465 <https://doi.org/10.11947/j.AGCS.2020.20200236>, 2020.
- 466 Kinoshita, Y.: Development of InSAR neutral atmospheric delay correction model by use of GNSS ZTD and  
467 its horizontal gradient, *IEEE T. Geosci. Remote.*, 60, 1-14,  
468 <https://doi.org/10.1109/TGRS.2022.3188988>, 2022.
- 469 Li, B., Ge, H., Bu, Y., Zheng, Y., and Yuan, L.: Comprehensive assessment of real-time precise products  
470 from IGS analysis centers, *Satellite Navigation*, 3, 12, <https://doi.org/10.1186/s43020-022-00074-2>,  
471 2022.
- 472 Li, R., Zhang, Z., Gao, Y., Zhang, J., and Ge, H.: A New Method for Deformation Monitoring of Structures  
473 by Precise Point Positioning, *Remote Sensing*, 15, 5743, <https://doi.org/10.3390/rs15245743>, 2023.
- 474 Li, S., Jiang, N., Xu, T., Xu, Y., Yang, H., Zhang, Z., Guo, A., and Wu, Y.: A precipitation forecast model  
475 with a neural network and improved GPT3 model for Japan, *GPS Solutions*, 27, 186,  
476 <https://doi.org/10.1007/s10291-023-01526-1>, 2023.
- 477 Li, X., Dick, G., Lu, C., Ge, M., Nilsson, T., Ning, T., Wickert, J., and Schuh, H.: Multi-GNSS meteorology:  
478 real-time retrieving of atmospheric water vapor from BeiDou, Galileo, GLONASS, and GPS  
479 observations, *IEEE T. Geosci. Remote.*, 53, 6385-6393,  
480 <https://doi.org/10.1109/TGRS.2015.2438395>, 2015.
- 481 Li, X., Wang, Q., Wu, J., Yuan, Y., Xiong, Y., Gong, X., and Wu, Z.: Multi-GNSS products and services at  
482 iGMAS Wuhan Innovation Application Center: Strategy and evaluation, *Satellite Navigation*, 3, 20,  
483 <https://doi.org/10.1186/s43020-022-00081-3>, 2022.



- 484 Lin, C. Y., Deng, Y., and Ridley, A.: Atmospheric gravity waves in the ionosphere and thermosphere during  
485 the 2017 solar eclipse, *Geophys. Res. Lett.*, 45, 5246-5252, <https://doi.org/10.1029/2018GL077388>,  
486 2018.
- 487 Liu, T., Zhang, B., Yuan, Y., and Li, M.: Real-Time Precise Point Positioning (RTPPP) with raw observations  
488 and its application in real-time regional ionospheric VTEC modeling, *J. Geodesy.*, 92, 1267-1283,  
489 <https://doi.org/10.1007/s00190-018-1118-2>, 2018.
- 490 Lu, C., Chen, X., Liu, G., Dick, G., Wickert, J., Jiang, X., Zheng, K., and Schuh, H.: Real-time tropospheric  
491 delays retrieved from multi-GNSS observations and IGS real-time product streams, *Remote Sensing*,  
492 9, 1317, <https://doi.org/10.3390/rs9121317>, 2017.
- 493 Lu, C., Li, X., Ge, M., Heinkelmann, R., Nilsson, T., Soja, B., Dick, G., and Schuh, H.: Estimation and  
494 evaluation of real-time precipitable water vapor from GLONASS and GPS, *GPS solutions*, 20, 703-  
495 713, <https://doi.org/10.1007/s10291-015-0479-8>, 2016.
- 496 Lu, C., Li, X., Nilsson, T., Ning, T., Heinkelmann, R., Ge, M., Glaser, S., and Schuh, H.: Real-time retrieval  
497 of precipitable water vapor from GPS and BeiDou observations, *J. Geodesy.*, 89, 843-856,  
498 <https://doi.org/10.1007/s00190-015-0818-0>, 2015.
- 499 Ma, X., Zhao, Q., Yao, Y., and Yao, W.: A novel method of retrieving potential ET in China, *J. Hydrol.*, 598,  
500 126271, <https://doi.org/10.1016/j.jhydrol.2021.126271>, 2021.
- 501 Pan, L., Deng, M., and Chen, B.: Real-time GNSS meteorology: a promising alternative using real-time PPP  
502 technique based on broadcast ephemerides and the open service of Galileo, *GPS Solutions*, 28, 113,  
503 <https://doi.org/10.1007/s10291-024-01659-x>, 2024.
- 504 Pan, L., and Guo, F.: Real-time tropospheric delay retrieval with GPS, GLONASS, Galileo and BDS data,  
505 *Sci. Rep.*, 8, 17067, <https://doi.org/10.1038/s41598-018-35155-3>, 2018.
- 506 Pipatsitee, P., Ninsawat, S., Tripathi, N. K., Shanmugam, M., and Chitsutti, P.: Estimating daily potential  
507 evapotranspiration using GNSS-based precipitable water vapor, *Heliyon*, 9,  
508 <https://doi.org/10.1016/j.heliyon.2023.e17747>, 2023.
- 509 Sha, Z., Hu, F., Wei, P., Ye, S., and Zhu, Y.: A method for calculating real-time ZTD grid data in Chinese  
510 regions based on GNSS ZTD modified ERA5 grid products, *J. Atmos. Sol.-Terr. Phy.*, 255, 106174,  
511 <https://doi.org/10.1016/j.jastp.2024.106174>, 2024.
- 512 Shu, B., Tian, Y., Qu, X., Li, P., Wang, L., Huang, G., Du, Y., and Zhang, Q.: Estimation of BDS-2/3 phase  
513 observable-specific signal bias aided by double-differenced model: an exploration of fast BDS-2/3  
514 real-time PPP, *GPS solutions*, 28, 1-14, <https://doi.org/10.1007/s10291-024-01632-8>, 2024.
- 515 StępniaK, K., Bock, O., Bossler, P., and Wielgosz, P.: Outliers and uncertainties in GNSS ZTD estimates from  
516 double-difference processing and precise point positioning, *GPS Solutions*, 26, 74,  
517 <https://doi.org/10.1007/s10291-022-01261-z>, 2022.
- 518 Su, C., Shu, B., Zheng, L., Tian, Y., Lei, T., Mu, X., and Wang, L.: Quality evaluation and PPP performance  
519 analysis of GPS/BDS real-time SSR products, *Geomatics and Information Science of Wuhan*  
520 University, <https://doi.org/10.13203/j.whugis20220760>, 2023.



- 521 Wang, D., Huang, G., Du, Y., Zhang, Q., Bai, Z., and Tian, J.: Stability analysis of reference station and  
522 compensation for monitoring stations in GNSS landslide monitoring, *Satellite Navigation*, 4, 29,  
523 <https://doi.org/10.1186/s43020-023-00119-0>, 2023.
- 524 Wang, L., Li, Z., Ge, M., Neitzel, F., Wang, Z., and Yuan, H.: Validation and assessment of multi-GNSS  
525 real-time precise point positioning in simulated kinematic mode using IGS real-time service,  
526 *Remote Sensing*, 10, 337, <https://doi.org/10.3390/rs10020337>, 2018.
- 527 Wang, Z., Li, Z., Wang, L., Wang, X., and Yuan, H.: Assessment of multiple GNSS real-time SSR products  
528 from different analysis centers, *ISPRS Int. J. Geo.-Inf.*, 7, 85, <https://doi.org/10.3390/ijgi7030085>,  
529 2018.
- 530 Xiong, Z., Zhang, B., and Yao, Y.: Comparisons between the WRF data assimilation and the GNSS  
531 tomography technique in retrieving 3-D wet refractivity fields in Hong Kong, *Ann. Geophys.*, 37,  
532 25-36, <https://doi.org/10.5194/angeo-37-25-2019>, 2019.
- 533 Yao, Y., He, Y., Yi, W., Song, W., Cao, C., and Chen, M.: Method for evaluating real-time GNSS satellite  
534 clock offset products, *GPS Solutions*, 21, 1417-1425, <https://doi.org/10.1007/s10291-017-0619-4>,  
535 2017.
- 536 Yao, Y., Luo, Y., Zhang, J., and Zhao, C.: Correlation analysis between haze and GNSS tropospheric delay  
537 based on coherent wavelet, *Geomatics and Information Science of Wuhan University*, 43, 2131-  
538 2138, <https://doi.org/10.13203/j.whugis20180234>, 2018.
- 539 Zhang, Z., Zeng, P., Wen, Y., He, L., and He, X.: Comprehensive assessment of BDS-2 and BDS-3 precise  
540 orbits based on B1I/B3I and B1C/B2a frequencies from iGMAS, *Remote Sensing*, 15, 582,  
541 <https://doi.org/10.3390/rs15030582>, 2023.
- 542 Zhu, G., Huang, L., Yang, Y., Li, J., Zhou, L., and Liu, L.: Refining the ERA5-based global model for vertical  
543 adjustment of zenith tropospheric delay, *Satellite Navigation*, 3, 27, [https://doi.org/10.1186/s43020-  
544 022-00088-w](https://doi.org/10.1186/s43020-022-00088-w), 2022.
- 545
- 546